Cavitation erosion in UHMWPE: a three-dimensional FEM study

Brunda Kattekola, Marc C. Fivel, Jean-Pierre Franc

Cavitation erosion in UHMWPE: A three-dimensional FEM study

Brunda Kattekola & Marc Fivel
Science et Ingénierie des Matériaux et Procédés (SIMaP-GPM2), University Grenoble Alpes/CNRS, Grenoble, France

Jean-Pierre Franc
Laboratoire des Ecoulements Géophysiques et Industriels (LEGI), University Grenoble Alpes/CNRS, Grenoble, France

ABSTRACT: In high velocity liquid flows, bubbles nucleate in regions of low pressure. These bubbles then grow to large size (often their final radius is many times greater than nucleation radius) and subsequently collapse in the high pressure region. Repeated implosions of these bubbles near a solid surface lead to significant surface damage and mass erosion. It has been experimentally observed that polymers such as Ultra-High Molecular Weight Polyethylene (UHMWPE) possesses a better resistance to cavitation erosion than Aluminium alloys and Bronze alloys and even stainless steels. In this numerical study, we perform a finite element study on the cavitation erosion in UHMWPE. In the first phase, a rate-dependent elastic-viscoelastic-viscoplastic constitutive model is calibrated to simulate the response of UHMWPE under different loading conditions and within a rather large range of strain rates (10^{-4} to $2000s^{-1}$). In the second phase, the effect of a single bubble collapse on a UHMWPE specimen investigated.

1 INTRODUCTION

Cavitation is a major cause of damage in solid parts that are subjected to high velocity flow conditions. During the high velocity flow, bubbles nucleate in regions where the pressure of the fluid is less than its vapor pressure. The bubbles grow and collapse in the high pressure region causing damage to the solid surface. It should be remarked that only the bubbles that collapse in the vicinity of the solid surface contribute to material damage. The collapse of bubbles may generate a shock wave or a re-entrant jet that is directed towards the solid surface. The manner of bubble collapse is governed by the distance between the bubble and the solid surface. At a distance greater than the radius of fully formed bubble, the bubble implosion generates a shock wave with an amplitude in the order of Gigapascals. A bubble much closer to the solid surface (due to an asymmetry in the form of presence of solid surface) would form a reentrant jet (or microjet) directed at the solid surface (Ewunkem 1993, Brennen 1995). Nevertheless, irrespective of method of bubble collapse, it should be noted, that a single bubble is capable of creating a pit i.e. a small plastic deformation on the material surface whereas repeated bubble implosions cause critical wear and mass loss at the solid surface. The surface damage is quantified by measuring the depth of the accumulated pits.

Cavitation damage has numerous implications in industrial context, hence there is a drive to develop materials that can minimize if not completely eliminate cavitation erosion. Experimental investigations, on the sintered samples of UHMWPE have shown that the resistance to cavitation erosion of UHMWPE is higher than some of its metallic counterparts for e.g.: Aluminum and Bronze alloys and Stainless steels A2205 (Deplancke et al. 2015). Furthermore, it has been observed that the resistance of UHMWPE to cavitation improves with increasing the molecular weight (Deplancke et al. 2015). This forms the thrust of the current numerical investigation where we simulate the cavitation erosion in UHMWPE of varying molecular weights.

Ultra High Molecular Weight Polyethylene (UHMWPE) belongs to commercially important class of semi-crystalline polymers. Its microstructure consists of two phases namely: amorphous and crystalline. When subjected to deformation, the two phases and their interaction with each other, gives the polymer a complex mechanical response. The response consists of several simultaneous deformation modes such as elastic, viscoelastic and viscoplastic. Further, when subjected to uniaxial tension, UHMWPE is known to exhibit post-yield strain softening followed by a strain hardening response. The stress-strain response further depends on loading rate, temperature etc. Given its complex response, numerous models (Hasan and Boyce 1993,

Bergstrm et al. 2002, Dommelen et al. 2003, Holmes et al. 2006, Pouriayevali et al. 2013) have been developed to capture the response of semi-crystalline polymers. Despite this fact, there are few models that can comprehensively characterize the polymer strain-strain response. In this study, we adopt a model that has an ability to simulate UHMWPEs response both in quasi-static and dynamic modes corresponding to isothermal and adiabatic conditions.

This paper is divided into four sections. In Section 2, we present the essential features of the rate-dependent consitutive model (Pouriayevali et al. 2013) and calibrate the model to simulate the mechanical response of UHMWPE. The experiments and numerical simulations of cavitation phenomenon are presented in Section 3. Further, in this section, we present the deformation induced in UHMWPE by a single dynamic bubble collapse. And finally, we conclude the paper with ungoing work and future plans.

2 CONSTITUTIVE MODEL

2.1 *Model description*

In this section, we briefly summarize the essential equations of the consitutive model, referring for a detailed description to (Pouriayevali et al. 2013).

The rheological representation of the constitutive model is shown in Figure 1. The model consists of two clusters arranged in series. The first cluster formed by a parallel combination of hyperelastic spring element 1 and Maxwell element governs the rate-dependent reversible elastic-viscoelastic deformation. The second cluster of friction slider-dashpot governs the rate-dependent irreversible deformation. The friction slider is activated at stress greater than the yield stress of the material. Further, the viscosities associated with the viscous flow are rate-dependent and there are few model parameters that account for the decrease in stiffness with temperature.

The free energy associated with the model is given by:

$$\psi = \psi_{\mathrm{e}} + \psi^{\mathrm{e}}_{\mathrm{ve}} \tag{1}$$

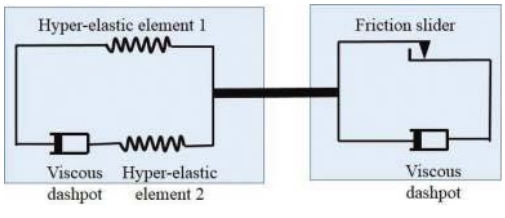

Figure 1. Rheological representation of elastic-viscoelastic-viscoplastic consitutive model.

where ψ_{e} and $\psi^{\mathrm{e}}_{\mathrm{ve}}$ correspond to the free energy of hyperelastic spring elements 1 and 2.

In the model, it is assumed that the free energies take a polynomial expression of the form:

$$\psi_{\mathrm{e}} = G_{\mathrm{e10}}(\overline{I}_{\mathrm{e1}} - 3) + G_{\mathrm{e01}}(\overline{I}_{\mathrm{e2}} - 3) + G_{\mathrm{e11}}(\overline{I}_{\mathrm{e1}} - 3)(\overline{I}_{\mathrm{e2}} - 3) + D_{\mathrm{e1}}(J_{\mathrm{e}} - 1)^2 \tag{2}$$

$$\psi^{\mathrm{e}}_{\mathrm{ve}} = G^{\mathrm{e}}_{\mathrm{ve10}}(\overline{I}^{\mathrm{e}}_{\mathrm{ve1}} - 3) + G^{\mathrm{e}}_{\mathrm{ve01}}(\overline{I}^{\mathrm{e}}_{\mathrm{ve2}} - 3) + G^{\mathrm{e}}_{\mathrm{ve11}}(\overline{I}^{\mathrm{e}}_{\mathrm{ve1}} - 3)(\overline{I}^{\mathrm{e}}_{\mathrm{ve2}} - 3) + D^{\mathrm{e}}_{\mathrm{ve1}}(J^{\mathrm{e}}_{\mathrm{ve}} - 1)^2 \tag{3}$$

where G_{e10}, G_{e01}, G_{e11}, $G^{\mathrm{e}}_{\mathrm{ve10}}$, D_{e1}, $G^{\mathrm{e}}_{\mathrm{ve01}}$, $G^{\mathrm{e}}_{\mathrm{ve11}}$ and $D^{\mathrm{e}}_{\mathrm{ve1}}$ are material parameters associated with the model. And the invariants $\overline{I}_{\mathrm{e1}}$, $\overline{I}_{\mathrm{e2}}$, J_{e} $\overline{I}^{\mathrm{e}}_{\mathrm{ve1}}$, $\overline{I}^{\mathrm{e}}_{\mathrm{ve2}}$ and $J^{\mathrm{e}}_{\mathrm{ve}}$ are associated with the elastic and viscoelastic parts of right Cauchy Green strain tensor $\overline{\mathbf{C}} = \overline{\mathbf{F}}^{\mathrm{T}}\overline{\mathbf{F}}$. Here $\overline{\mathbf{F}}$ is the distortional part of the deformation gradient tensor.

In the absence of heat flux and source, the free energy satisfies the Clausius-Duhem inequality, i.e.:

$$\mathbf{S} : \frac{1}{2}\dot{\mathbf{C}} - \dot{\psi} - \eta\dot{\theta} \geq 0 \tag{4}$$

where $\mathbf{S}$ is the second Piola-Kirchoff stress, $\mathbf{C} = \mathbf{F}^{\mathrm{T}}\mathbf{F}$ is right Cauchy Green strain tensor, η is entropy and θ is absolute temperature. All quantities are defined per unit reference volume.

The expressions for stress and flow rules are derived by making an assumption that under all conditions, the rate of entropy change is positive. Closed form expression of stress can be found in Pouriayevali et al. 2013. For the sake of completion, flow rules are included below.

The viscoelastic and viscoplastic flow rules are given by:

$$\mathbf{D}^{v}_{\mathrm{ve}} = \frac{\| \mathbf{T}^{0}_{\mathrm{ve}} \|}{\mu^{\mathrm{D}}_{\mathrm{ve}}} \mathbf{N}_{\mathrm{ve}} \tag{5}$$

and

$$\mathbf{D}_{\mathrm{p}} = \frac{\| \mathbf{T}^{0} \|}{\mu^{\mathrm{D}}_{\mathrm{p}}} \mathbf{N}_{\mathrm{p}} \tag{6}$$

where, $\mu^{\mathrm{D}}_{\mathrm{ve}}$ and $\mu^{\mathrm{D}}_{\mathrm{p}}$ are viscosities associated with viscoelastic and viscoplastic flow. Further, the driving stress to inelastic flow are given by $\mathbf{T}^{0}_{\mathrm{ve}}$ and $\mathbf{T}^{0}$ with $\mathbf{N}_{\mathrm{ve}}$ and $\mathbf{N}_{\mathrm{p}}$ as respective directions.

The viscoplastic flow rule is modified to incorporate an yield criterion as well as post-yield deformation behavior:

$$\mathbf{D}_{\mathrm{p}} = \frac{< f\left(\mathbf{T}^{0}, \sigma_{y} + \varepsilon\right) >}{\mu^{\mathrm{D}}_{\mathrm{p}}} \mathbf{N}_{\mathrm{p}} \tag{7}$$

where the yield surface is defined as:

$$f\left(\mathbf{T}^0, \sigma_y + \varepsilon\right) = \|\mathbf{T}^0\| - \sqrt{\frac{2}{3}}(\sigma_y + \varepsilon) \tag{8}$$

where, σ_y is the yield stress of the material and ε is the hardening function of exponential function of the form $\varepsilon = H(exp(\| \mathbf{E}_a \|^Q) - 1)$. The Almansi plastic strain is further computed as $\mathbf{E}_a = (I - \mathbf{B}_p)/2$. $\mathbf{B}_p$ is the plastic part of the left Cauchy Green strain tensor ($\mathbf{B} = \mathbf{F}\mathbf{F}^T$). The model parameters H and Q govern the strain softening and hardening regimes.

2.2 *Model calibration*

Uniaxial tensile and compression experiments were conducted on dogbone and cylindrical specimens respectively. During the experiments, the loading rate as well as the molecular weights were varied. The constitutive model has 17 parameters whose values were determined from the uniaxial experimental stress-strain data. The parameters corresponding to each element are demonstrated in Figure 2.

Three dimensional Finite-Element simulations were performed on ABAQUS v6.11. The constitutive model described in the previous section was implemented as user subroutined VUMAT. For the purpose of consistency, the geometry and boundary conditions from experiments was replicated in simulations.

The parameters G_{eij} and D_{ei} associated with spring element 1 are related to shear G and bulk modulus K of the material according to the relationship:

$$\sum_{i,j=1}^{n} G_{eij} = G/2 \tag{9}$$

and

$$\sum_{i=1}^{n} D_{ei} = K/2 \tag{10}$$

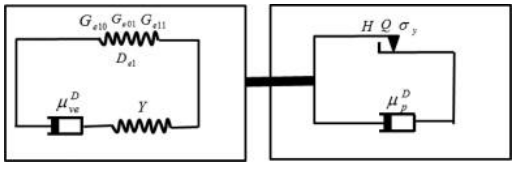

Figure 2. Rheological representation of elastic-viscoelastic-viscoplastic constitutive model with the list of parameters concerning each of the elements.

Further, it is also assumed that the constants associated with hyperelastic element 2 (ref: Fig. 1) are given by $G^e_{vij} = YG_{eij}$

To compute the yield stress σ_y, tangents are drawn to elastic-viscoelastic and yield regimes. The stress at the intersection of the tangents is chosen as yield stress parameter.

The remainder of the parameters are determined from iterations such that the error between experiments and simulated curves is minimal. In Figures 3 and 4, the uniaxial response of UHMWPE from simulations (solid lines) is overlaid on experimental response (dashed lines). It can be seen from Figure 3 that with increasing molecular weight,

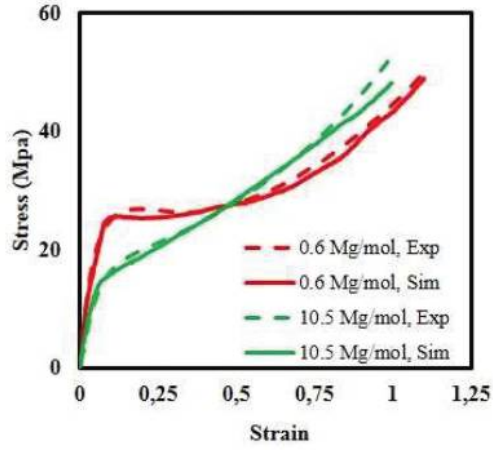

Figure 3. Uniaxial response of UHMWPE in tension from numerical simulations (solid lines) are superposed on experimental data (dashed line).

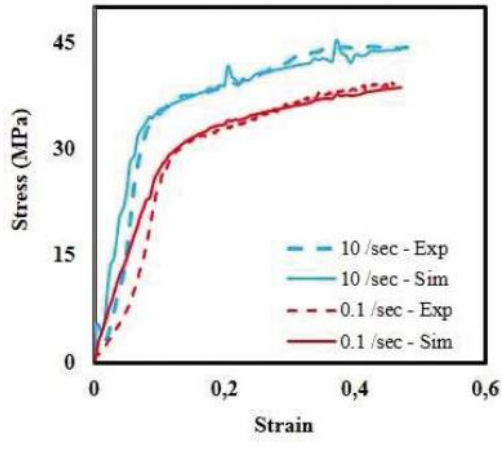

Figure 4. Uniaxial response of UHMWPE in compression from numerical simulations (solid lines) are superposed on experimental data (dashed line).

UHMWPE yields at lower stress. Further, the necking in the specimen which manifests itself as strong peak in the yield is sharper at the lower molecular weight.

3 CAVITATION

3.1 *Experiments*

In Figure 5, the experimental setup for performing the cavitation tests is demonstrated. And in Figure 6, a picture of the circular specimen holder of 10 cm diameter is shown. The specimen holder contains six slots, that are used to place cylindrical specimens that can be simultaneously tested for cavitation erosion. More details on specimen preparation can be found in (Deplancke et al. 2015). The specimen holder with six specimens is placed in a hydrodynamic tunnel where all the specimens are subjected to a jet of water at 90 m/s flow velocity. As mentioned before, only the bubbles collapsing in the vicinity of solid surface contribute to damage.

The pictorial evidence of cavitation erosion can be presented in Figure 6, where six UHMWPE

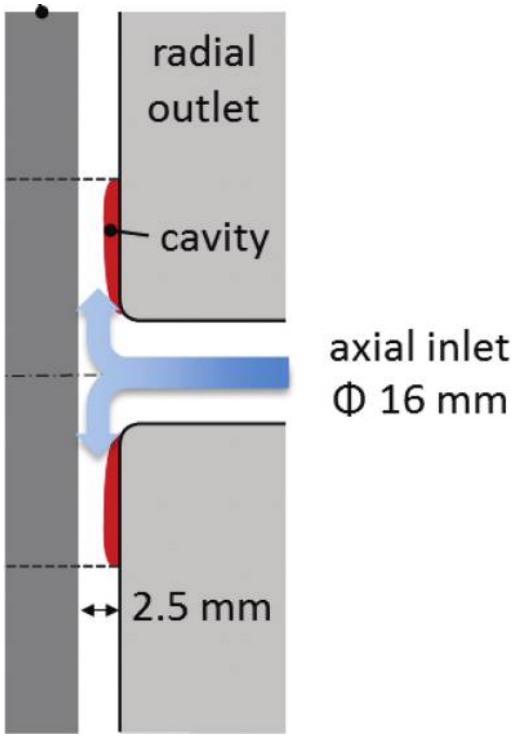

Figure 5. Schematic of experimental setup for performing cavitation tests. The image is taken from Reference 3.

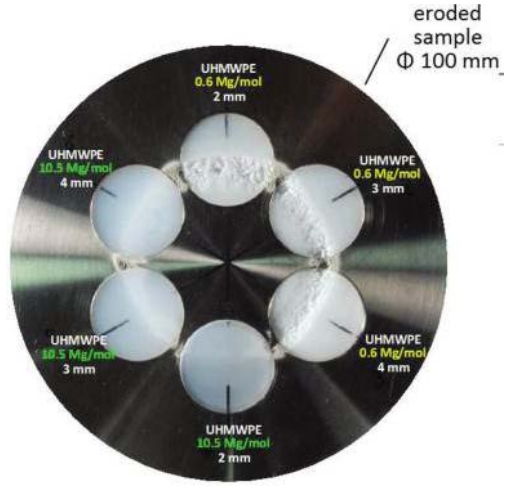

Figure 6. Image showing the surface erosion in six UHMWPE cylindrical plate specimens of varying thicknesses and molecular weights when subjected to water jet at 90 m/s flow velocity for 100 hours. The image is taken from Reference 3.

cylindrical plate specimens of varying thicknesses and molecular weights have been for cavitation erosion for 100 hours in water jet with flow velocity 90 m/s. The specimens of lower molecular weight i.e. 0.6 Mg/mol experience much larger erosion compared to those with 10.5 Mg/mol molecular weight. Further, no evidence of thickness was observed either from images or profilometry measurements (Deplancke et al. 2015).

3.2 *Numerical simulations*

3.2.1 *Geometry and boundary conditions*

Utilizing the symmetry of the cylindrical specimens, the numerical simulations were performed on an axisymmetric plate. The finite element mesh in the $\theta = 0$ plane is shown in Figure 7. The mesh is coarser at the far ends and much refined at the north-west corner where load boundary conditions are applied. The 4 noded axisymmetric element CAX4R were used to discretize the geometry.

A Gaussian form of pressure distribution is applied at the top surface (Kim et al. 2014). On the top surface, the applied pressure pulse is of the form:

$$\sigma = \sigma_{\mathrm{H}} \exp\left(-\left(\frac{r}{r_{\mathrm{H}}} \right)^2 \right) \tag{11}$$

where r is the radius of the cylindrical plate, r_{H} and σ_{H} loading parameters. In the current investigation,

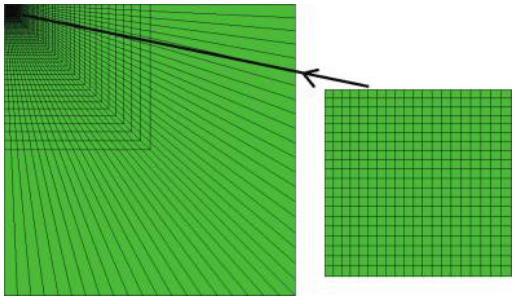

Figure 7. Finite element mesh on the axisymmetric plate. The mesh in the north-west corner is much refined.

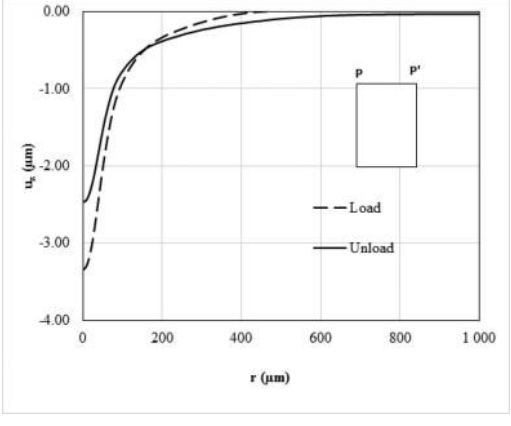

Figure 8. Axial displacement of a line $P - P'$ for σ_H = 20 MPa. The 'load' and 'unload' curves correspond to displacement at $\sigma = \sigma_H$ and to $\sigma = 0$ MPa.

the value of r_H has been held constant at 50 μm and σ_H is varied from 20 MPa to 200 MPa.

At the center line ($r = 0$, z), the displacement in the radial direction u_r is constrained, i.e.:

$$u_r = 0 \tag{12}$$

and at the bottom of the plate (r, $z = 0$), the displacement in the axial direction, u_z is constrained, i.e.:

$$u_z = 0 \tag{13}$$

3.2.2 *Primary results*

In Figures 8 and 9, the axial displacement u_z along a line $P - P'$ (shown in the inset of Figs. 8 and 9) is plotted for σ_H = 20 MPa and 200 MPa respectively. Further, the dashed line in both the figures corresponds to the instance when the applied pressure at point P attains a maximum value of $\sigma = \sigma_H$. The applied pressure is then gradually reduced to

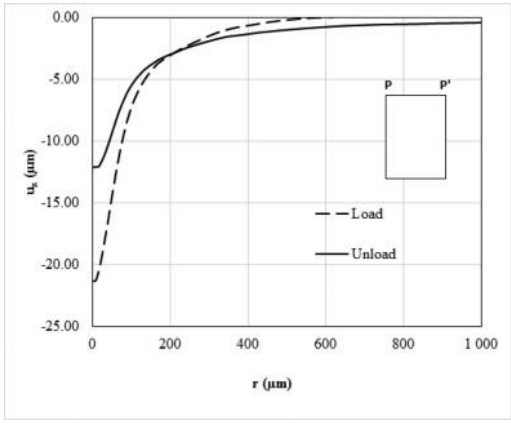

Figure 9. Axial displacement of a line $P - P'$ for σ_H = 200 MPa. The 'load' and 'unload' curves correspond to displacement at $\sigma = \sigma_H$ and $\sigma = 0$ MPa.

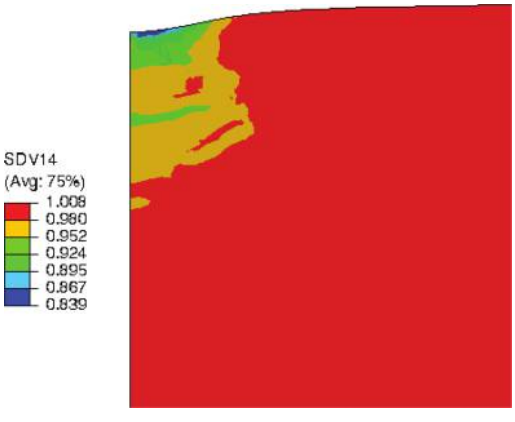

Figure 10. Contours of viscoelastic part of deformation gradient tensor at an instant when applied pressure σ is reduced to zero for the case σ_H = 200 MPa.

zero and the inelastic displacement at that instant is plotted in solid lines with label 'unload'. At $\sigma_H < \sigma_y$, the specimen is restored to undeformed configuration. It can be seen that the elastic part of the deformation is quickly recovered, however, the recovery of the viscoelastic deformation takes longer time. The time taken for restoration strongly depends on parameters governing the Maxwell element (see Fig. 2).

The contours of viscoelastic and plastic parts of deformation gradient tensor are plotted in Figures 10 and 11 at the instant when the applied pressure σ is gradually reduced from $\sigma = \sigma_H$ to zero. It can be seen from Figure 10 that the viscoelastic deformation has not been fully recovered even

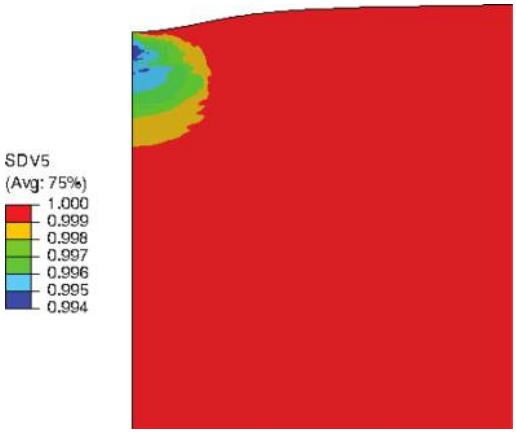

Figure 11. Contours of plastic part of deformation gradient tensor at an instant when applied pressure σ is reduced to zero for the case $\sigma_H = 200$ MPa.

after a complete unloading of the specimen. From the contours of the plastic deformation gradient tensor (Fig. 11), it is clear that the magnitude of plastic deformation is greatest at a region below the point suffering maximum displacement. So, if a failure were to initiate, it would most likely be in the interior of the specimen.

4 CONCLUSIONS

In this work, we have numerically simulated a plastic pit analysis with no mass loss in UHMWPE with molecular weight 0.6 Mg/mol at different magnitudes of pressure pulse. It is seen that with increasing load, the pit depth increases. Although not reported in the paper, it has been observed, during unloading, the time required to recover elastic-viscoelastic deformation is very closely related to the viscosity parameters.

The magnitude of the applied pressure pulse is 200 MPa which is much lower than what is predicted from experiments. However, it should be observed that UHMWPE is a compliant material (as opposed to metals that are almost perfectly rigid). As a result, the amplitude of cavitation impact loads on UHMWPE is expected to be smaller than that on metals. This is due to the fluid-structure interaction, not modeled here. Roy et al. 2014 used a finite element based inverse algorithm to determine the magnitudes and distribution of the pressure load that would be required to cause a pre-defined pit depth. It is expected that polymers would be subjected to pressure of the order of 1GPa.

Excessive distortion of mesh prevents us from increasing the magnitude σ_H the of pressure pulse. We are currently exploring, Coupled Eulerian Lagrangian Analysis capability in ABAQUS v6.11 to avoid severe mesh distortion.

Finally, the investigation will include the effect of molecular weight on resistance to cavitation erosion.

ACKNOWLEDGEMENTS

Authors would like to thank Office of Naval Research, USA for providing the necessary financial assistance.

REFERENCES

Bergstrm, J.S., S.M. Kurtz, C.M. Rimnac, & A.A. Edidin (2002). Constitutive modeling of ultra-high molecular weight polyethylene under large-deformation and cyclic loading conditions. *Biomaterials 23*, 2329–2343.

Brennen, C.E. (1995). *Cavitation and bubble dynamics*. Oxford University Press.

Deplancke, T., O. Lame, J.-Y. Cavaille, M. Fivel, J.-P. Franc, & M. Riondet (2015). Outstanding cavitation erosion resistance of ultra high molecular weight polyethylene (uhmwpe) coatings. *Wear 328*, 301–308.

Dommelen, V., J. van, D.M. Parks, M.C. Boyce, W.A.M. Brekelmans, & F.P.T. Baaijens (2003). Micromechanical modeling of the elasto-viscoplastic behavior of semicrystalline polymers. *Journal of the Mechanics and Physics of Solids 51*(3), 519–541.

Ewunkem, A. (1993). *Cavitation erosion of engineering materials*. City University London.

Hasan, O.A. & M.C. Boyce (1993). Energy storage during inelastic deformation of glassy polymers. *Polymer 34*, 5085–5092.

Holmes, D.W., J.G. Loughran, & H. Suehrcke (2006). Constitutive model for large strain deformation of semicrystalline polymers. *Mechanics of Time-Dependent Materials 10*(4), 281–313.

Kim, K.-H., G. Chahine, J.-P. Franc, & A. Karimi (2014). *Advanced Experimental and Numerical Techniques for Cavitation Erosion Prediction*.

Pouriayevali, H., S. Arabnejad, Y. Guo, & V. Shim (2013). A constitutive description of the rate-sensitive response of semi-crystalline polymers. *International Journal of Impact Engineering 62*, 35–47.

Roy, S., M. Fivel, J.-P. Franc, & C. Pellone (2014). Cavitation induced damage: Fem inverse modeling of the flow aggressiveness. *Proceedings of Eleventh International Conference on Flow Dynamics*.